RESEARCH ARTICLE

Thermoelectric properties and Kondo transition in the pseudo-gap metals TiNiSi and TiNiGe

Ruth A. Downie,[a] Blair F. Kennedy,[a] Rajan Biswas,[b] Ronald I. Smith,[c] and Jan-Willem G. Bos*[b]

Materials with the TiNiSi structure have recently been highlighted as potential thermoelectric materials. Here we report the thermoelectric properties of TiNiX (X=Si and Ge). Both materials behave as defective metals or heavily doped degenerate semiconductors. Room temperature Seebeck coefficients are $-45\ \mu V K^{-1}$ (Si) and $-20\ \mu V K^{-1}$ (Ge) with electrical resistivities of 0.5–1 mΩcm. The lattice thermal conductivities are 8 W m^{-1}K^{-1} (Si) and 6 W m^{-1}K^{-1} (Ge) at 360 K, which is promising in the absence of alloying. The calculated power factors and figures of merit remain small, with the largest $S^2/\rho = 0.17$ mW m^{-1}K^{-2} and peak $zT = 5 \times 10^{-3}$ seen in TiNiSi near 300 K. Both compositions show Kondo behaviour at low-temperatures, linked to the emergence of local moment magnetism, and have substantial magnetoresistance effects at 2 K. This work provides property characterisation for two members of this large class of intermetallic materials.

1. Introduction

Thermoelectric materials can be used in power generation from waste heat, small mW scale energy harvesting and in Peltier heat pumps.[1] The efficiency of a thermoelectric material is given by its figure of merit, $zT = (S^2/\rho\kappa)T$, where S is the Seebeck coefficient, ρ the electrical resistivity, $\kappa = \kappa_{lat} + \kappa_{el}$ is the sum of the lattice and electronic thermal conductivities, and T is the absolute temperature. Amongst the many groups of thermoelectric materials under current investigation,[2] intermetallic ABC compositions with the half-Heusler structure have attracted considerable interest.[3] This is because they have a favourable combination of good performance, mechanical properties, stability and are based on abundant elements. Half-Heusler compositions (e.g. TiNiSn) can be understood using Zintl electron counting, with ionic Ti^{4+} and zincblende $[NiSn]^{4-}$ structural components, which yields semiconducting behaviour for 18 valence electrons.[3a,4] However, there is another large group of ABC intermetallic compounds with the TiNiSi structure-type.[5] Bandstructure calculations from open source resources (e.g. the Materials Project)[6] show that these materials have a pseudogap near the Fermi level, which is characteristic for semimetals. The predicted semimetallic behaviour suggests that these materials have limited potential use as thermoelectrics, as semiconductors are normally required.[1] However, recent computational materials exploration has suggested that some compositions with this structure type (including TiNiSi) may afford good zT values.[7] This has led to reports on the thermoelectric performance of TiNiSi,[8] and ZrNiX (X=Si, Ge),[9] i.e. the Zr analogues of the materials studied here. So far none of these shows large zT values, as compositions remain too metallic, but further exploration is of interest. In the broader class of Heusler materials, semimetallic Fe_2VAl (a 24-electron system) has recently been demonstrated to have very large power factors $S^2/\rho \sim 10$ mW m^{-1}K^{-2} near room temperature.[10] This indicates that semimetals with favourable bandstructures can support good electrical performance.

The TiNiSi-type structure is orthorhombic with $Pnma$ space group.[5] Ni and X bond to form layers of 6-membered rings in a graphitic-type arrangement, as demonstrated in Figure 1(a). These layers are puckered, as illustrated by the side-on view in Figure 1(b). They stack along the a-axis and are interlinked, with Ni–X bonds forming 4-membered rings between the layers. The Ti cations occupy the space between the layers in the channels that run the length of the a-axis. To a first approximation, the TiNiX structure comprises a covalently bound $[NiX]^{n-}$ lattice that forms ionic bonds to Ti^{n+} cations. In reality, however, calculations show that Ti does not fully transfer its valence electrons to the [NiX] sublattice.[5] The bonding is therefore intermediate between ionic and covalent.

Examples of the ABC TiNiSi-structure exist where A can be any of the first-row transition metals and B can also be varied greatly.[5,11] This results in a large number of different compositions and properties. In ANiSi compositions, for example, Pauli paramagnetism has been observed where A=Sc–V, whilst ferromagnetism has been reported for compositions where A=Cr–Fe.[5] In some compositions where B is a second or third row

[a] R. A. Downie, B. F. Kennedy
Institute of Chemical Sciences, School of Engineering and Physical Sciences, Heriot-Watt University, Edinburgh, UK, EH14 4AS
[b] R. Biswas, J.-W. G. Bos
EaStCHEM School of Chemistry, University of St Andrews, St Andrews, UK, KY16 9ST
E-mail: jwb2@st-andrews.ac.uk
[c] R. I. Smith
ISIS Facility, Rutherford Appleton Laboratory, Harwell Oxford, Didcot, UK, OX11 0QX
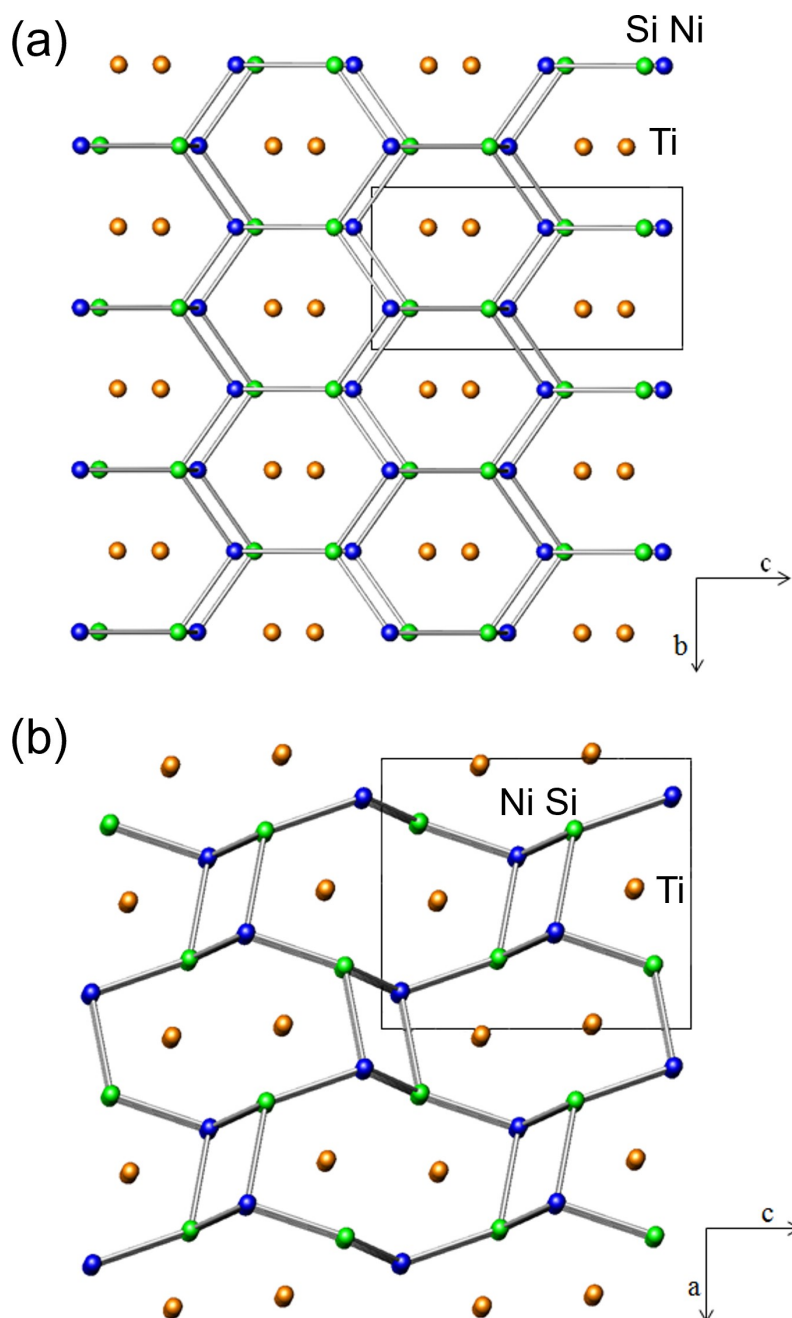
Figure 1. Schematic representation of the TiNiSi structure; **(a)** viewed along the a-axis illustrating the puckered hexagonal [NiSi] net and **(b)** viewed along the b-axis illustrating the connecting Ni_2Si_2 4-ring linkers.

transition metal, superconductivity has been observed: $T_c = 2.3$ K was reported for HfRhSi;[12] and $T_c = 3.5$ K was found in TaPtSi.[13] In addition, to the recent literature, there are some older studies reporting on the thermoelectric properties of this structure-type. A study of CePtSn, CeNiSn, CeRhSb and CeRhAs revealed high $S(T)$ along with relatively low $\rho(T)$, below room temperature.[14]

The compositional flexibility of the TiNiSi structure affords the possibility to combine thermoelectricity with magnetism. Magnetic thermoelectrics, where magnetic effects lead to

enhanced $S(T)$ are of considerable interest to improve performance.[15] In the early 2000s, this focused on strongly correlated systems, largely cobalt oxides,[16] where spin and orbital degeneracy yield large $S(T)$ in metallic systems. More recently, paramagnetic fluctuations have been implicated in enhanced $S(T)$ in semiconductors.[15] Examples include para-magnon drag in MnTe,[17] and enhanced $S(T)$ in Fe_2VAl,[18] $CuGaTe_2$,[19] and Bi_2Te_3[20] doped with magnetic elements. Magnetic thiospinels $Cu(CrTi)S_4$[15,21] and $Sr_2Fe_{1+x}Re_{1-x}O_6$ double

perovskite oxides were also found to show magneto-thermo-electric effects.[22]

Here, we present the results of an investigation into the crystal structure, including Rietveld analysis of neutron powder diffraction data of TiNiSi, and the high-temperature thermo-electric and low-temperature transport properties of the TiNiX (X = Si, Ge) compositions. This work compliments existing work on TiNiSi and reports new characterisation of TiNiGe.

2. Experimental

TiNiSi was prepared on a 5-g scale by arc-melting stoichiometric quantities of elemental starting powders purchased from Alfa Aesar (all > 99.99% purity). No further annealing was undertaken as this resulted in degradation of the sample. TiNiGe was also prepared by arc-melting, and in this case, the ingot was then vacuum sealed in a quartz tube and annealed at 900 °C for 3 days. Laboratory powder X-ray diffraction (XRD) data were collected on a Bruker D8 Advance diffractometer (Cu K_α, $\lambda = 1.54056$ Å). Neutron powder diffraction (NPD) data for TiNiSi was collected on the Polaris instrument at the ISIS facility, Rutherford Appleton Laboratory, UK. Room temperature data were collected up to a total of 300 µA hr proton beam current. Rietveld refinement of all collected diffraction data was performed using the GSAS suite of programs.[23] Scanning electron microscopy (SEM) and Energy Dispersive X-ray Spectroscopy (EDS) elemental maps were collected using a Quanta 650 FEG SEM equipped with an Oxford Instruments X-max 150 N detector. Quantitative analysis of selected areas was performed using the Aztec Large Area Maps software. $S(T)$ and $\rho(T)$ above room temperature were measured using a Linseis LSR-3 instrument. $\kappa(T)$ was measured using an Anter Flashline 3000 flash diffusion instrument using a Pyroceram reference sample. The temperature dependences of field and zero-field cooled magnetic susceptibilities were measured in a 1 T applied field using a Quantum Design MPMS. Low temperature $\rho(T)$ and magnetoresistance $R(H)/R_0$ measurements were carried out using a Quantum Design PPMS. Resistance measurements were performed in the standard 4-probe geometry.

3. Structure

TiNiSi: Laboratory XRD confirmed formation of the TiNiSi phase, with no observable impurities. NPD was subsequently carried out and the Rietveld fits to the collected data for banks 4 and 5 are presented in Figure 2a. Lattice parameters, atomic positions, site occupancies, thermal parameters and selected bond angles and distances are collated in Table 1, along with the fit statistics for the refinement. The orthorhombic TiNiSi structure was found to fit the data well.[5,24] Refinement of the site occupancies suggest a small ~1% deficiency on the Ti and Ni sites (Table 1). However, the site occupancy values correlate with the thermal displacement parameters, so it is likely that TiNiSi is stoichiometric. Inspection of the Ni–Si–Ni and Si–Ni–Si bond angles reveals that none of these measure 109.5°, which is the bond angle for ideal tetrahedra. They also deviate substantially from the 120° angle found in a perfect honeycomb lattice, highlighting the puckered nature of the graphitic-type layers. The bond angles in this layer are illustrated in Figure 3(a). The 4-membered rings that link the layers are distorted and do not form a perfect square, with the Ni–Si–Ni angle measuring

Table 1. Lattice and atomic parameters, selected bond angles and distances and fit statistics for the Rietveld fits to neutron diffraction data for TiNiSi and X-ray diffraction data for TiNiGe. Ti, Ni and X each occupy a (x, $\frac{1}{4}$, z) site. * indicates the angles within the puckered graphitic layers. **indicates angles that make up the 4-membered rings linking the graphitic layers.

		TiNiSi	TiNiGe
a (Å)		6.15380(6)	6.2446(1)
b (Å)		3.66984(4)	3.7487(1)
c (Å)		7.02172(7)	7.1471(1)
Ti	Occ	0.989(3)	1
	U_{iso} (Å^2)	0.0038(1)	0.0072(6)
	x	0.02236(9)	0.0253(3)
	z	0.68085(8)	0.6826(2)
Ni	Occ	0.986(2)	1
	U_{iso} (Å^2)	0.00453(6)	0.0148(6)
	x	0.14153(3)	0.1361(3)
	z	0.06003(3)	0.0591(3)
Si/Ge	Occ	1	1
	U_{iso} (Å^2)	0.0042(1)	0.0114(4)
	x	0.26596(8)	0.2563(3)
	z	0.37750(6)	0.3778(2)
Ni–X (Å)		2.3577(5)	2.399(2)
		2.3091(3)	2.375(1)
		2.3523(5)	2.414(2)
Ni–X–Ni (°)		127.21(1)*	127.33(5)*
		119.68(2)	118.99(8)
		105.24(2)*	104.20(9)*
		69.79(1)**	67.69(6)**
X–Ni–X (°)		116.398(9)*	115.44(5)*
		98.22(1)	97.47(7)
		105.243(2)*	104.20(9)*
		110.22(1)**	112.31(6)**
χ^2		5.8	4.0
Bank 5	wR_p	1.9	13.9
	R_p	2.6	10.2
	R_f^2	1.6	13.0
Bank 4	wR_p	1.6	–
	R_p	2.9	–
	R_f^2	3.0	–
Bank 3	wR_p	2.4	–
	R_p	3.5	–
	R_f^2	9.1	–

69.79(1)° and the Si–Ni-Si angle measuring 110.22(1)°. This distortion maximises the distance between the Si atoms, which are more electronegative than Ni,[5] as illustrated in Figure 3 (b).

TiNiGe: Inspection of the XRD pattern collected for this sample confirmed formation of TiNiSi-type TiNiGe as the major phase in the sample.[25] However, a further set of 4–5 fairly intense peaks are present in this sample (Figure 2b). These could not be indexed by any of the known elemental, binary or ternary phases reported in the Ti–Ni–Ge phase diagram.[26] SEM and EDS mapping revealed the presence of small amounts of
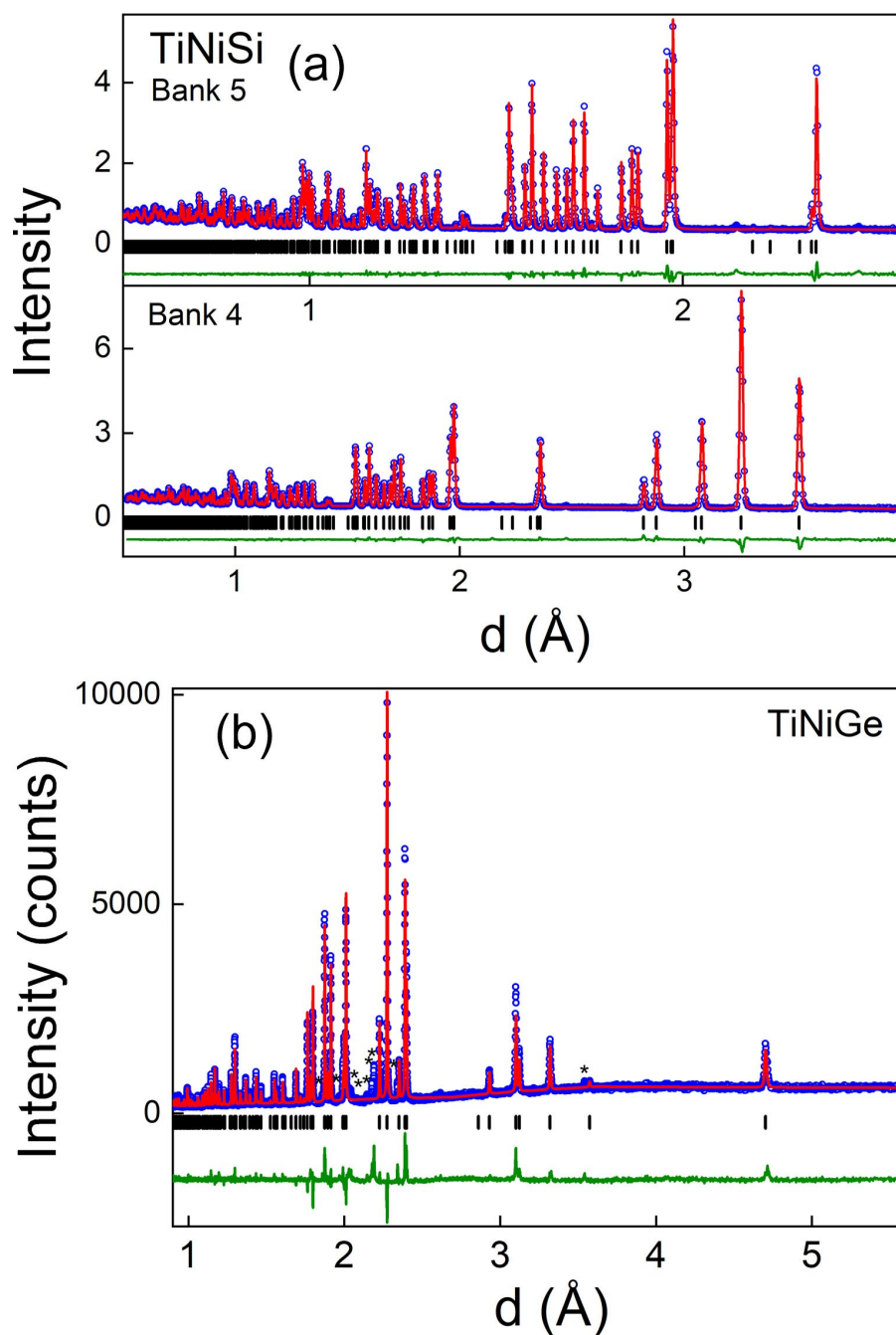
Figure 2. (a) Rietveld fit to Polaris neutron powder diffraction data for TiNiSi. (b) Rietveld fit to laboratory X-ray powder diffraction data for TiNiGe. Data: blue circles; fitted model: red line; difference curve: green line. Markers are for the Bragg positions of the TiNiX phase. (*) mark the unidentified impurity peaks in TiNiGe.

Ni_3Ge_2 and Ti_5Ge_3 (Figures S1, S2 and Table S1). The latter is present in the XRD data with a fitted phase fraction of 1.3(1) wt%. Ni_3Ge_2 is not observed in the XRD data and could be present as an amorphous phase.[26] The origin of the unindexed peaks at d = 3.54 Å, d = 2.34 Å, d = 2.19 Å, d = 2.18 Å and d = 2.04 Å is currently not known. It has been reported that the TiNiSi structure-type often competes with the ZrNiAl structure,[27] but this phase does not readily index the additional reflections. From SEM-EDS, the majority of the sample is

homogenous with a 1:1:1 composition. We speculate that these additional peaks are therefore either a second phase with similar 1:1:1 composition, or that TiNiGe is distorted, leading to a lower symmetry structure. A structural distortion would also explain the relatively poor fit of the intensities of some of the reflections, which is not due to texturing. The final Rietveld fit to the X-ray data is shown in Figure 2b and the refined structural parameters are summarised in Table 1. The unit cell is expanded compared to TiNiSi, as expected because of the
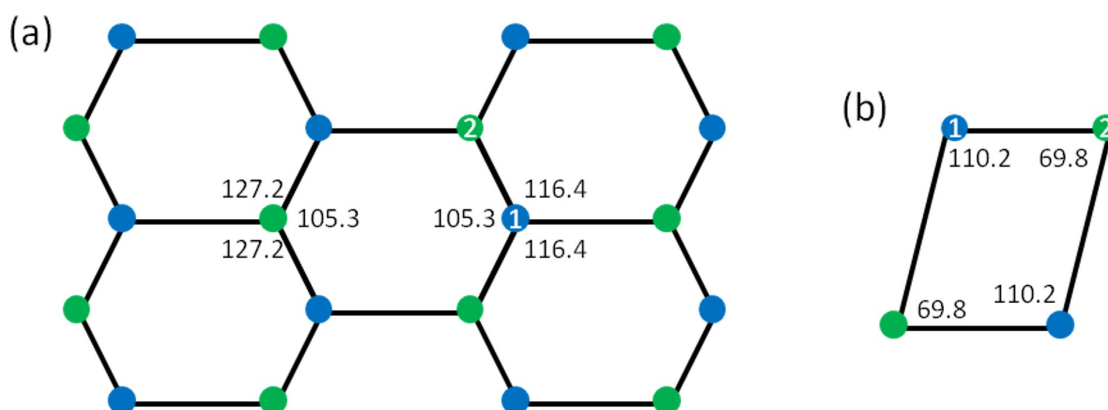
Figure 3. Bond angles in **(a)** the puckered [NiSi] layers and **(b)** the 4-membered rings that link the layers. Blue circles are Ni and green are Si.

larger size of Ge. The Ni—Ge bond distances show a corresponding increase. Five out of six of the bond angles within the 6-membered rings are decreased upon comparison with the NiSi layers, indicating increased puckering of the layers. This is likely driven by the lengthening of the Ge—Ge distance in the 4-membered ring.

4. Properties

4.1 High temperature thermoelectric properties: The 300–740 K thermoelectric properties of the TiNiX compositions are shown in Figure 4. The $S(T)$ for both samples are negative, indicating n-type conduction (Figure 4a). The magnitudes are low, with $S_{300K} = -45\ \mu V K^{-1}$ for X = Si and $S_{300K} = -20\ \mu V K^{-1}$ for X = Ge. The $\rho(T)$ are consistent with metal-like behaviour (Figure 4b). The magnitudes are indicative of semimetallic (or heavily doped semiconducting) behaviour, with $\rho_{300K} = 1\ m\Omega\,cm$ for X = Si and $\rho_{300K} = 0.6\ m\Omega\,cm$ for X = Ge.

The $\kappa(T)$ and $\kappa_{lat}(T)$ for TiNiSi and TiNiGe are shown in Figure 4c, d. The total κ is dominated by κ_{lat}, despite the substantial electronic contribution for these highly conducting samples. Here $\kappa_{el} = LT/\rho = 2-3\ W\,m^{-1}\,K^{-1}$ was calculated using the Lorenz number $L = 2.44 \times 10^{-8}\ V^{-2}\,K^{-2}$ for a metal. The $\kappa_{lat, 360K} = 8\ W\,m^{-1}\,K^{-1}$ for TiNiSi, decreasing to $5\ W\,m^{-1}\,K^{-1}$ at 775 K. The heavier Ge analogue has slightly lower values, with $\kappa_{lat, 360K} = 6\ W\,m^{-1}\,K^{-1}$, decreasing to $4\ W\,m^{-1}\,K^{-1}$ at 775 K. Both samples show an upturn in $\kappa(T)$ at high temperatures, suggesting the onset of p-type minority carrier transport, which is also evident in $S(T)$. The magnitude of κ_{lat} is lower than that for defect-free TiNiSn, which has $\kappa_{lat} = 12\ W\,m^{-1}\,K^{-1}$ at 300 K.[28] This suggests that the increased structural complexity of the TiNiX (X = Si, Ge) phases outweighs their lower average atomic mass. Interstitial Ni is known to lead to a dramatic reduction of κ_{lat} in TiNiSn based compositions,[28–29] but there is no evidence from diffraction for interstitial Ni (or substantial Ni vacancies) in the TiNiX compounds. The fit to the NPD dataset accounts for the observed intensities, suggesting that the average TiNiSi structure is an accurate description of the material structure.

However, as discussed below, both TiNiX samples are characterised by a large residual resistivity ρ_0, suggesting a substantial amount of structural disorder.

The power factors remain modest with $S^2/\rho = 0.18\ mW\,m^{-1}\,K^{-2}$ and $0.06\ mW\,m^{-1}\,K^{-2}$ at 300 K for TiNiSi and TiNiGe, respectively (Figure 4e). The S^2/ρ does not vary much with temperature for X = Ge, whilst it decreases for X = Si, with the best performance near 300 K. Measurement of S^2/ρ below 300 K would be of interest for TiNiSi.

The low $S(T)$ and relatively large $\kappa(T)$ (compared to high zT materials), severely limits the calculated figures of merit (Figure 4f). A highest $zT = 5 \times 10^{-3}$ is reached for TiNiSi at 300 K, whilst TiNiGe has a relatively constant $zT = 2 \times 10^{-3}$ over the measured temperature range.

4.2 Low temperature resistivity and magnetoresistance: the 2–350 K $\rho(T)$ and magnetoresistance $MR = R(H)/R_0$ at 2 K are shown in Figure 5. The measured $\rho(T)$ are consistent with the high temperature values (Figure 4b, 5a). Similar to the high temperature data, there is limited temperature dependence with calculated residual resistivity ratios, $RRR = \rho_{350K}/\rho_{2K} = 1.5$ for TiNiSi and $RRR = 2.9$ for TiNiGe. This is typical for bad metals and highly doped semiconductors, where disorder and/or impurities cause electron scattering and large ρ_0 at T = 0 K. The measured ρ_{2K} values are $0.7\ m\Omega\,cm$ for X = Si and $0.2\ m\Omega\,cm$ for X = Ge. The TiNiSi sample changes to semiconducting $\rho(T)$ on cooling below 50 K and has a broad ρ "hump" between 175–250 K. The TiNiGe sample shows a similar transition to semiconducting behaviour below 20 K. The broad $\rho(T)$ hump is reminiscent of a charge density wave, where nesting causes (part of) the Fermi surface to be gapped, leading to an increase in ρ. This typically only occurs in lower-dimensional materials (e.g. layered TiSe$_2$).[30] However, the pseudo-gap nature of TiNiSi may make this material susceptible to such a transition. If this occurs, there should be a related structural distortion that can be probed using diffraction. The low-temperature semiconducting $\rho(T)$, coupled to a finite resistivity at 0 K, is indicative of a Kondo transition, where charge carriers incur an additional resistive contribution due to scattering from magnetic impurities.[31] Gapped or mobility-limited semiconductors show
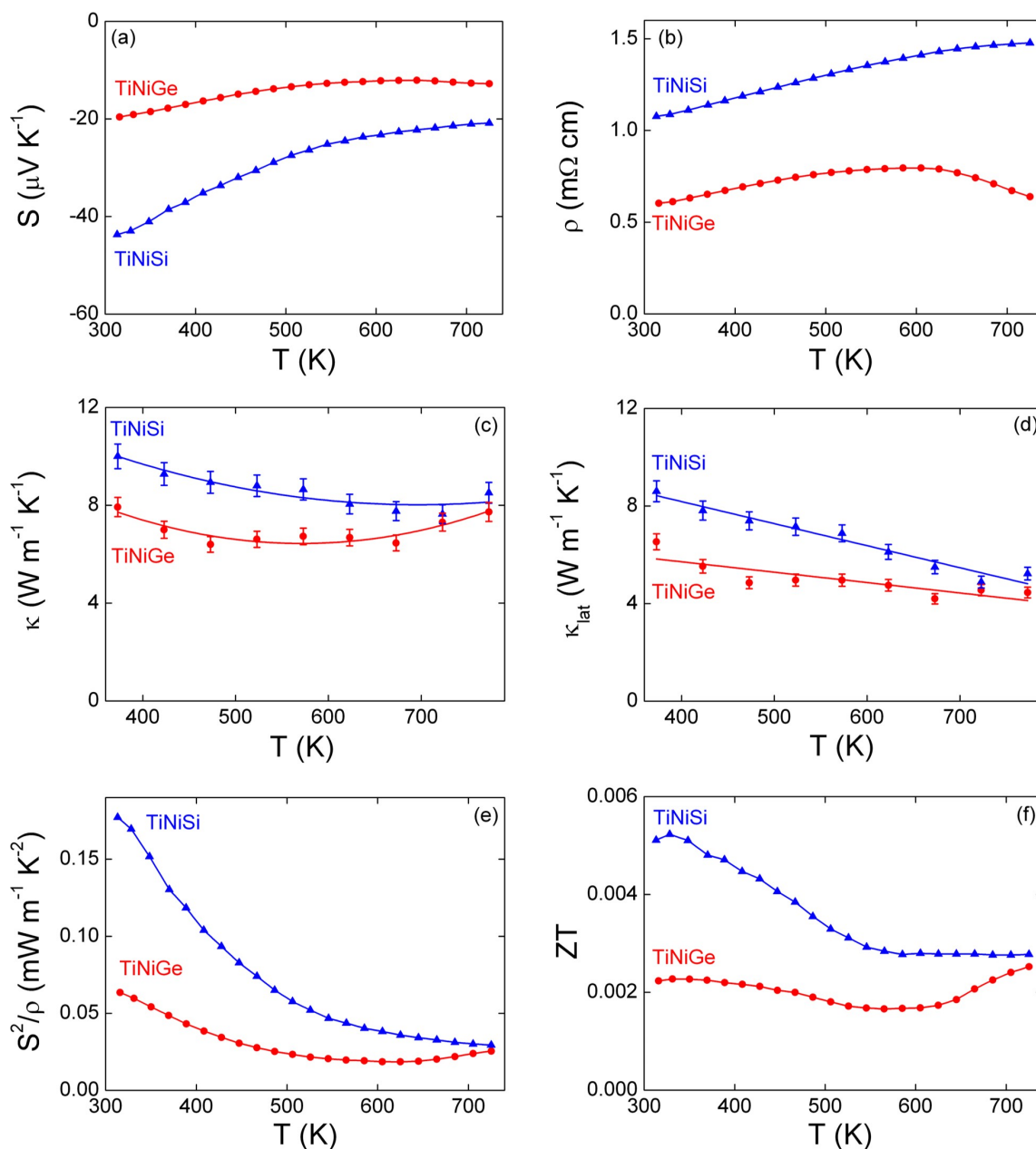
Figure 4. Temperature dependences of the **(a)** Seebeck coefficient (S), **(b)** electrical resistivity (ρ), **(c)** total thermal conductivity (κ), **(d)** lattice thermal conductivity (κ_{lat}), **(e)** thermoelectric power factor (S^2/ρ) and **(f)** figure of merit, zT for TiNiSi and TiNiGe.

a diverging $\rho(T)$ on cooling. To test this hypothesis, the $\rho(T)$ data were fitted to the following expression:[32]

$$\rho(T) = \rho_{imp,\,0} + AT^2 + BT^5 + \rho_{K,0}\left(\frac{1}{1 + (2^{1/s} - 1)(T/T_K)^2}\right)^s \quad (1)$$

Here, $\rho_{imp,0}$ is the 0 K resistivity due to non-magnetic impurity scattering, the second and third terms are due to electron-electron and electron-phonon scattering, and the final term is the Kondo resistivity (ρ_K). The parameter $s = 0.225$ for a $S = \frac{1}{2}$ system.[32] $\rho_{K,0}$ is the 0 K resistivity due to magnetic impurities and T_K is the Kondo temperature, which gives the

energy scale of the magnetic impurity scattering. The final fits to the 2–120 K $\rho(T)$ data are shown in Figure 5b, and the fit parameters are given in Table 2. Overall, the quality of the fit is very good, suggesting that the semiconducting upturn is indeed due to Kondo scattering. It clearly describes the $\rho(T)$ minimum and the saturation of $\rho(T)$ as T→0 K. The fits yield $T_K = 93(3)$ K for X=Si and $T_K = 69(7)$ K for X=Ge. These temperatures coincide with the onset of significant deviations from Pauli paramagnetism in the magnetic susceptibility data (section 4.3). The ratio of $\rho_{K,0}/\rho_{imp,0} = 0.34$–0.39, signalling a similar contribution of magnetic impurity scattering, despite the
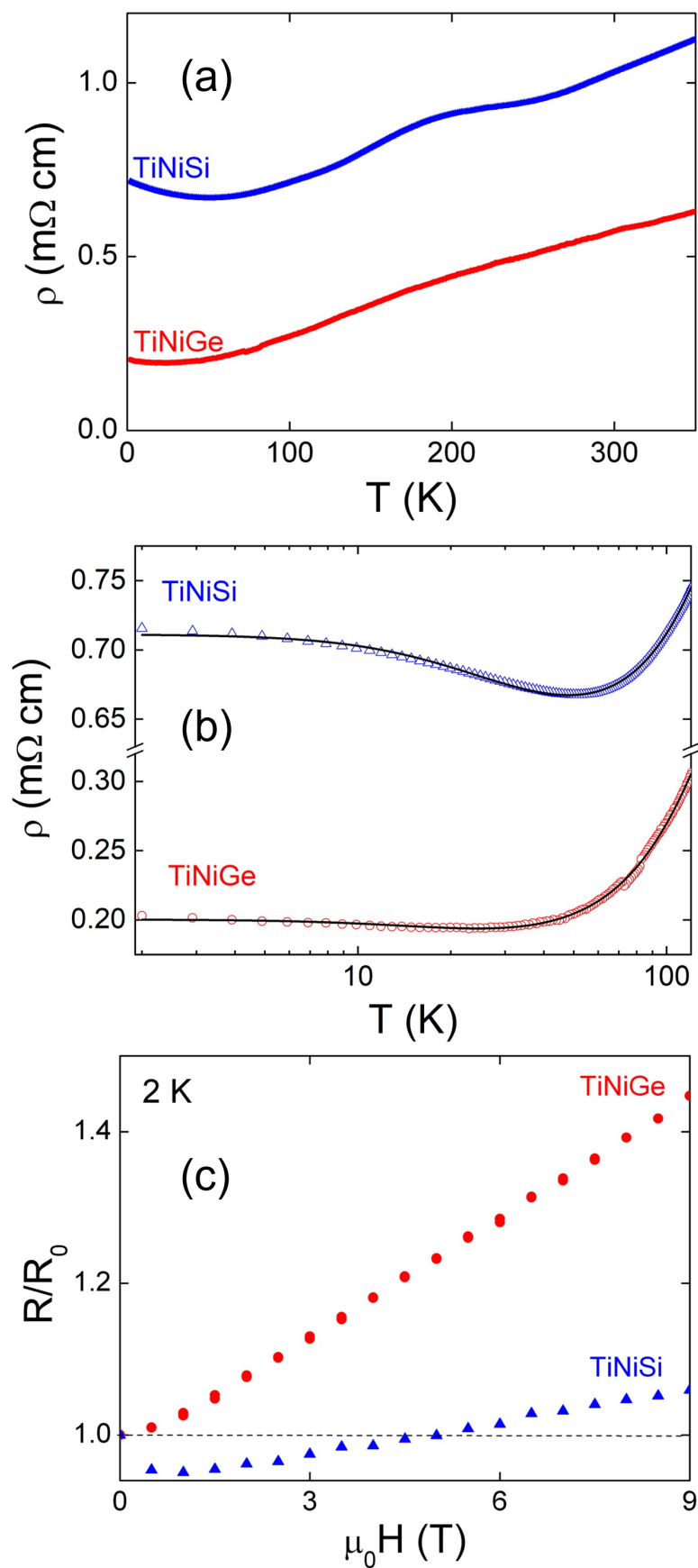
Figure 5. Low-temperature electrical properties for TiNiSi and TiNiGe: **(a)** Temperature dependence of the electrical resistivity (ρ), **(b)** fits using the Kondo model (eqn. 1 in the manuscript) and **(c)** Magnetoresistance (R/R_0) at 2 K.

© 2023 The Authors. Zeitschrift für anorganische und allgemeine Chemie published by Wiley-VCH GmbH

Table 2. Overview of the fitted parameters used to describe the low-temperature electrical resistivity and the magnetic susceptibility of the TiNiX samples (X = Si, Ge).

	X = Si	X = Ge
ρ_0 (mΩ cm)	0.512(5)	0.149(4)
A (mΩ cm K^{-2})	$1.08(2) \times 10^{-5}$	$1.04(2) \times 10^{-5}$
B (mΩ cm K^{-5})	$-4.7(6) \times 10^{-13}$	$-5.6(6) \times 10^{-13}$
$\rho_{K,0}$ (mΩ cm)	0.199(4)	0.051(4)
$\rho_{K,0}/\rho_0$	0.39	0.34
T_K (K)	93(3)	69(7)
χ_0 (emu mol^{-1} Oe^{-1})	$6.98(1) \times 10^{-5}$	$7.99(1) \times 10^{-5}$
C (emu mol^{-1} Oe^{-1}K)	$2.5(1) \times 10^{-4}$	$5.41(5) \times 10^{-4}$
θ (K)	$-4.1(2)$	$-1.8(1)$

much lower overall ρ and less pronounced Kondo minimum for TiNiGe.

The two samples show different MR, with a large positive response of +44% for TiNiGe (in a 9 T field). By contrast, for TiNiSi, initially negative MR is observed, which changes to a positive response above 1 T (Figure 5c). The overall change in MR between the minimum at 1 T and 9 T is +10%. Regular metals show positive MR (usually on the order of a few %) as conduction electrons are deflected by the applied magnetic field. The magnitude of the positive MR observed here is therefore somewhat large in comparison with good metals, but

in line with measurements on other degenerate semiconductors.[33] The cause of the change from negative to positive MR in TiNiSi is unclear at present, but could be linked to the observation of a stronger Kondo effect in this sample.

4.3 Magnetic Properties: Magnetic susceptibility (χ) measurements are presented in Figure 6. Both samples show low χ values that are independent of temperature over most of the measured temperature range, indicating Pauli paramagnetism. This is in agreement with early work on TiNiGe,[25] which reports this composition as Pauli paramagnetic. Each sample also exhibits a paramagnetic tail due to local magnetic moments at low temperatures. The $\chi(T)$ was fitted using the following expression:

$$\chi(T) = \chi_0 + \frac{C}{T - \theta} \tag{2}$$

Here, χ_0 is the Pauli paramagnetic contribution, and the Curie-Weiss law (the second term) is used to describe the local moments that emerge on cooling. This expression gives a good fit to $\chi(T)$ over the 2–300 K interval (Figure 6). The final fit parameters are summarised in Table 2. The obtained Curie constants (C) and Weiss temperatures (θ) are $C = 2.5(1) \times 10^{-4}$ emu Oe^{-1} mol^{-1} K and $\theta = -4.1(2)$ K (Si) and $C = 5.4(1) \times 10^{-3}$ emu Oe^{-1} mol^{-1}K and $\theta = -1.8(1)$ K (Ge). This indicates the presence of a small fraction of magnetic impurities that have
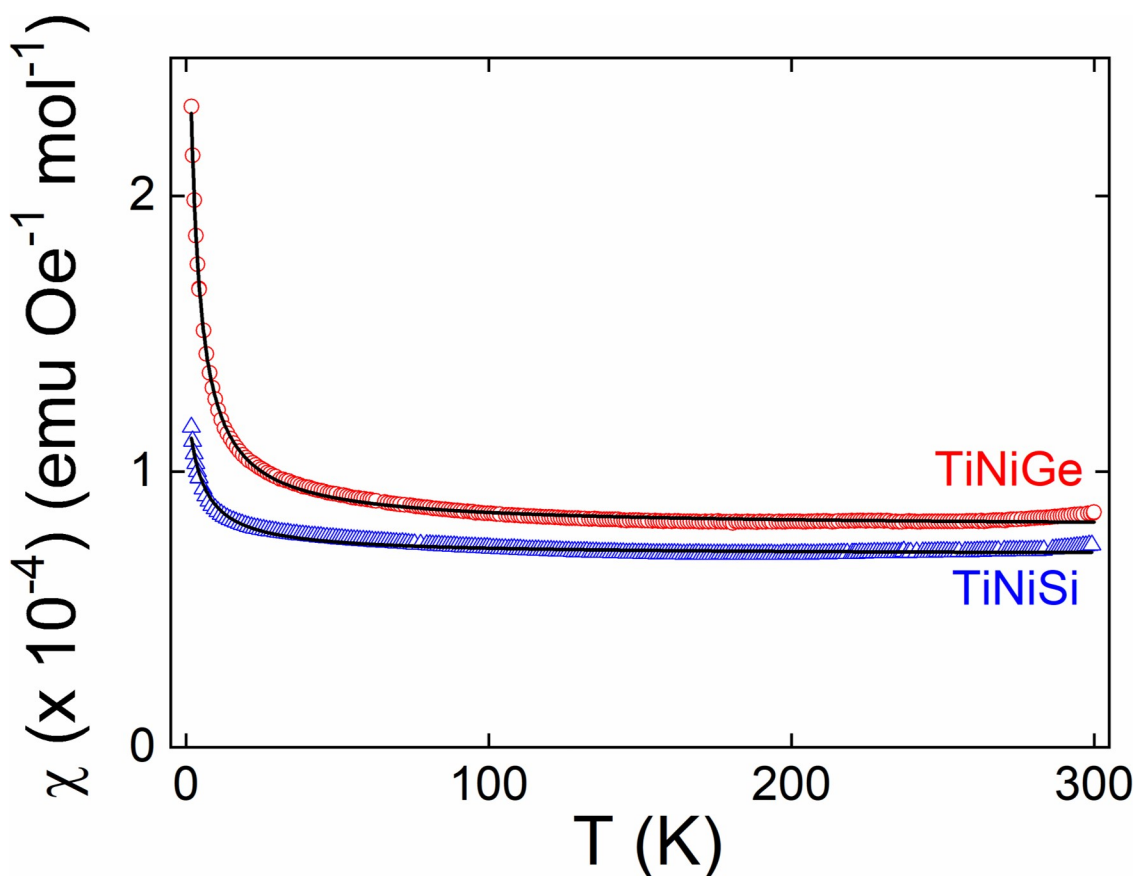

Figure 6. Temperature dependence of the magnetic susceptibility for TiNiSi and TiNiGe. The solid lines are fits using eqn. 2.

weak antiferromagnetic interactions. These local moments could be due to foreign magnetic dopants (e.g. Fe, Co replacing Ni) or be linked to defects (e.g. Ni vacancies, site inversion) in the TiNiX structure. Assuming that the magnetic moment arises from unpaired electrons with spin $S = 1/2$, the observed C correspond to a concentration of ~0.1% magnetic defects ($C = 0.375$ emu Oe^{-1} mol^{-1} K for 1 mole of $S = 1/2$ defects). The small θ are consistent with weakly interacting dilute magnetic impurities located within the main phase. From the observation of the Kondo effect in $\rho(T)$, these magnetic defects are coupled to the electronic transport.

5. Discussion

TiNiSi and TiNiGe were prepared using arc melting and characterised without further processing, such as milling and hot pressing or spark plasma sintering. In agreement with previous studies, both were found to adopt the orthorhombic TiNiSi-type structure.[5] TiNiSi was found to be almost phase pure and stoichiometric, within the error of the site occupancy refinement. The TiNiGe sample was found to contain a major phase with the TiNiSi-type structure but contained a number of unindexed reflections. SEM-EDS showed the presence of minor amounts of Ni_3Ge_2 and Ti_5Ge_3 but importantly shows that most of the material has a 1:1:1 composition. This suggests that either a symmetry lowering distortion has occurred or that the sample contains a second phase with equimolar composition.

Maximum zT values were found to be 5×10^{-3} at room temperature for TiNiSi and 2.5×10^{-3} at 725 K for TiNiGe. These values are low for thermoelectric applications, for reference TiNiSn prepared using the same synthesis approach, reaches $zT = 0.7$ at 740 K.[29] However, it may be possible to increase the performance as suggested by recent theoretical work.[7] This should focus on improving $S(T)$ and the thermoelectric power factor (S^2/ρ) as without improvement to the electrical properties, high zT values will remain out of reach. If improvements can be achieved, then reductions in κ_{lat} can be targeted. The performance of our TiNiSi sample is comparable to the literature ($zT = 6 \times 10^{-3}$ at 800 K), with V substitution leading to a performance increase to $zT = 0.035$ at 600 K, largely driven by an increase in $S(T)$.[8] Work on ZrNiSi demonstrated a similar peak $zT = 0.02$ at 700 K in samples doped n-type with Sb (and $zT = 5 \times 10^{-3}$ at 900 K for ZrNiSi).[9a] In the literature studies on TiNiSi and ZrNiSi, n-type doping improved $S(T)$ but overall S^2/ρ remains modest, not exceeding 0.5 mW m^{-1} K^{-2}, and peak $S(T)$ values near -40 μV K^{-1}.[8–9] From the perspective of semiconductor thermoelectrics, this trend is unexpected, as increasing doping levels usually leads to a decrease in S. A ZrNiSi sample with simultaneous Sb doping and Hf alloying on the Ti site, reached $zT = 0.06$ at 950 K. The combined impact of Sb doping and Hf alloying reduced κ_{lat} from 11 W m^{-1} K^{-1} to 3 W m^{-1} K^{-1}, demonstrating that low κ are possible in this structure type.[9a] The literature TiNiSi and ZrNiSi samples do not show the increase in $S(T)$ on cooling that our sample shows, and measurement of zT below 300 K would be of interest.

A possible route towards performance improvements is to tune the crystal structure towards the LiGaGe-type structure, which has planar graphitic layers, i.e. to remove the puckering of the [NiX] layers in our materials. This approach has been experimentally demonstrated for CaAgSb, which transforms upon rare-earth substitution, enhancing zT to 0.7 at 1080 K.[34] Another possibility is to use disorder tuning to create a narrow impurity band, which is the approach used to enhance S in the Fe_2VAl-based Heusler compositions.[10]

The observation of large ρ_0 values and low RRR (suggesting large concentration of defects) are typical for poor metals with a high degree of impurity scattering. The observation of Kondo behaviour, local moment magnetism and substantial MR effects suggest that the TiNiX (X = Si, Ge) materials could display substantial magneto-thermoelectric effects, and this could be a focus for future work. The observation of the broad hump in $\rho(T)$ for TiNiSi also warrants further investigation.

To conclude, we have reported on the basic transport properties of TiNiSi and TiNiGe, analogues to the much-studied TiNiSn half-Heusler alloy. This shows that they are limited by poor electronic thermoelectric responses. Opening of a band-gap in these materials should improve their performance. The low-temperature properties of these materials are interesting with the observation of Kondo behaviour and deserve more attention.

Author Statement

Synthesis (R.A.D); Data acquisition and analysis (R.A.D., B.F.K., R. B. and J.W.G.B.); Manuscript writing - original draft (R.A.D.); Conceptualisation, funding, project supervision, manuscript writing - review & editing (J.W.G.B.).

Acknowledgements

Conflict of Interest

The authors declare no conflict of interest.

Data Availability Statement

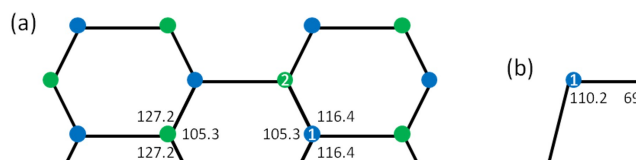The research data underpinning this publication can be accessed at https://doi.org/10.17630/99214eaf-bdbd-431b-98d2-890b25f2c2d6.

RESEARCH ARTICLE

[1] a) R. Funahashi, Woodhead Publishing, **2021**; b) D. M. Rowe, in *Materials, Preparation, and Characterization in Thermoelectrics*, CRC Press, Boca Raton, **2012**, pp. 1–553.

[2] a) Q. Yan, M. G. Kanatzidis, *Nat. Mater.* **2022**, *21*, 503–513; b) X.-L. Shi, J. Zou, Z.-G. Chen, *Chem. Rev.* **2020**, *120*, 7399–7515; c) T. Hendricks, T. Caillat, T. Mori, *Energies* **2022**, *15*, 7307; d) G. Tan, M. Ohta, M. G. Kanatzidis, *Philos. Trans. R. Soc. London Ser. A* **2019**, *377*, 20180450; e) Y. Zheng, T. J. Slade, L. Hu, X. Y. Tan, Y. Luo, Z.-Z. Luo, J. Xu, Q. Yan, M. G. Kanatzidis, *Chem. Soc. Rev.* **2021**, *50*, 9022–9054.

[3] a) R. J. Quinn, J.-W. G. Bos, *Materials Advances* **2021**, *2*, 6246–6266; b) J.-W. G. Bos, in *Thermoelectric Energy Conversion* (Ed.: R. Funahashi), Woodhead Publishing, **2021**, pp. 125–142; c) S. J. Poon, *Journal of Physics D-Applied Physics* **2019**, *52*, 493001; d) W. G. Zeier, J. Schmitt, G. Hautier, U. Aydemir, Z. M. Gibbs, C. Felser, G. J. Snyder, *Nat. Rev. Mater.* **2016**, *1*, 16032; e) T. Zhu, C. Fu, H. Xie, Y. Liu, X. Zhao, *Adv. Energy Mater.* **2015**, *5*, 1500588; f) J. W. G. Bos, R. A. Downie, *J. Phys. Condens. Matter* **2014**, *26*, 433201.

[4] T. Graf, C. Felser, S. S. P. Parkin, *Prog. Solid State Chem.* **2011**, *39*, 1–50.

[5] G. A. Landrum, R. Hoffmann, J. Evers, H. Boysen, *Inorg. Chem.* **1998**, *37*, 5754–5763.

[6] A. Jain, S. P. Ong, G. Hautier, W. Chen, W. D. Richards, S. Dacek, S. Cholia, D. Gunter, D. Skinner, G. Ceder, K. A. Persson, *APL Mater.* **2013**, *1*, 011002.

[7] C. Barreteau, J.-C. Crivello, J.-M. Joubert, E. Alleno, *ACS Comb. Sci.* **2020**, *22*, 813–820.

[8] Y. Huang, H. Nagai, K. Hayashi, Y. Miyazaki, *J. Alloys Compd.* **2019**, *771*, 111–116.

[9] a) K. Saurabh, A. Kumar, P. Ghosh, S. Singh, *Physical Review Materials* **2022**, *6*, 065401; b) K. Saurabh, A. Kumar, P. Ghosh, S. Singh, *Physical Review Materials* **2021**, *5*, 085406.

[10] a) F. Garmroudi, M. Parzer, A. Riss, A. V. Ruban, S. Khmelevskyi, M. Reticcioli, M. Knopf, H. Michor, A. Pustogow, T. Mori, E. Bauer, *Nat. Commun.* **2022**, *13*, 3599; b) F. Garmroudi, M. Parzer, A. Riss, S. Beyer, S. Khmelevskyi, T. Mori, M. Reticcioli, E. Bauer, *Materials Today Physics* **2022**, *27*, 100742.

[11] S. V. Ackerbauer, A. Senyshyn, H. Borrmann, U. Burkhardt, A. Ormeci, H. Rosner, W. Schnelle, M. Gamża, R. Gumeniuk, R. Ramlau, E. Bischoff, J. C. Schuster, F. Weitzer, A. Leithe-Jasper, L. H. Tjeng, Y. Grin, *Chem. Eur. J.* **2012**, *18*, 6272–6283.

[12] I. Shirotani, Y. Konno, Y. Okada, C. Sekine, S. Todo, T. Yagi, *Solid State Commun.* **1998**, *108*, 967.

[13] S. Yashiro, A. Kasahi, R. Kasai, H. Samata, Y. Nagata, *J. Alloys Compd.* **2000**, *309*, 51–56.

[14] T. Takabatake, T. Sasakawa, J. Kitgawa, T. Suemitsu, Y. Echizen, K. Umeo, M. Sera, Y. Bando, *Physica B +C* **2003**, *328*, 53–57.

[15] S. Hébert, R. Daou, A. Maignan, S. Das, A. Banerjee, Y. Klein, C. Bourgès, N. Tsujii, T. Mori, *Sci. Technol. Adv. Mater.* **2021**, *22*, 583–596.

[16] a) P. Limelette, S. Hebert, V. Hardy, R. Fresard, C. Simon, A. Maignan, *Phys. Rev. Lett.* **2006**, *97*, 046601; b) A. Maignan, V. Caignaert, B. Raveau, D. Khomskii, G. Sawatzky, *Phys. Rev. Lett.* **2004**, *93*, 026401; c) A. C. Masset, C. Michel, A. Maignan, M. Hervieu, O. Toulemonde, F. Studer, B. Raveau, J. Hejtmanek, *Phys. Rev. B* **2000**, *62*, 166–175; d) J. Sugiyama, J. H. Brewer, E. J. Ansaldo, H. Itahara, T. Tani, M. Mikami, Y. Mori, T. Sasaki, S. Hebert, A. Maignan, *Phys. Rev. Lett.* **2004**, *92*, 017602; e) J. W. G. Bos, J. T. Hertz, E. Morosan, R. J. Cava, *J. Solid State Chem.* **2007**, *180*, 3211–3217.

[17] Y. Zheng, T. Lu, M. M. H. Polash, M. Rasoulianboroujeni, N. Liu, M. E. Manley, Y. Deng, P. J. Sun, X. L. Chen, R. P. Hermann, D. Vashaee, J. P. Heremans, H. Zhao, *Sci. Adv.* **2019**, *5*, eaat9461.

[18] N. Tsujii, A. Nishide, J. Hayakawa, T. Mori, *Sci. Adv.* **2019**, *5*, eaat5935.

[19] F. Ahmed, N. Tsujii, T. Mori, *J. Mater. Chem. A* **2017**, *5*, 7545–7554.

[20] a) J. B. Vaney, S. Aminorroaya Yamini, H. Takaki, K. Kobayashi, N. Kobayashi, T. Mori, *Materials Today Physics* **2019**, *9*, 100090; b) J. W. G. Bos, M. Lee, E. Morosan, H. W. Zandbergen, W. L. Lee, N. P. Ong, R. J. Cava, *Phys. Rev. B* **2006**, *74*, 184429.

[21] D. Berthebaud, O. I. Lebedev, A. Maignan, S. Hebert, *J. Appl. Phys.* **2018**, *124*, 063905.

[22] a) S. Hébert, R. Carbonio, C. Martin, A. Maignan, *Z. Anorg. Allg. Chem.* **2023**, *649*, e202200324; b) A. Maignan, C. Martin, O. Lebedev, J. Sottmann, L. Nataf, F. Baudelet, S. Hébert, R. E. Carbonio, *Chem. Commun.* **2019**, *55*, 5878–5881.

[23] a) L. B. McCusker, R. B. von Dreele, D. E. Cox, D. Louer, P. Scardi, *J. Appl. Crystallogr.* **1999**, *32*, 36–50; b) B. H. Toby, *J. Appl. Crystallogr.* **2001**, *34*, 210–213.

[24] C. B. Shoemaker, D. P. Shoemaker, *Acta Crystallogr.* **1965**, *18*, 900–905.

[25] W. Bażela, A. Szytula, *physica status solidi* **1981**, *66*, 45–52.

[26] Z. Y. Xie, K. L. Lv, Y. H. Luo, H. S. Liu, Z. P. Jin, *J. Alloys Compd.* **2015**, *645*, 344–351.

[27] A. O. Oliynyk, L. A. Adutwum, B. W. Rudyk, H. Pisavadia, S. Lotfi, V. Hlukhyy, J. J. Harynuk, A. Mar, J. Brgoch, *J. Am. Chem. Soc.* **2017**, *139*, 17870–17881.

[28] S. A. Barczak, J. Buckman, R. I. Smith, A. R. Baker, E. Don, I. Forbes, J.-W. G. Bos, *Materials* **2018**, *11*, 536.

[29] R. A. Downie, D. A. MacLaren, R. I. Smith, J. W. G. Bos, *Chem. Commun.* **2013**, *49*, 4184–4186.

[30] E. Morosan, H. W. Zandbergen, B. S. Dennis, J. W. G. Bos, Y. Onose, T. Klimczuk, A. P. Ramirez, N. P. Ong, R. J. Cava, *Nat. Phys.* **2006**, *2*, 544–550.

[31] J. Kondo, *Prog. Theor. Phys.* **1964**, *32*, 37–49.

[32] a) T. A. Costi, A. C. Hewson, V. Zlatic, *J. Phys. Condens. Matter* **1994**, *6*, 2519; b) D. Goldhaber-Gordon, J. Göres, M. A. Kastner, H. Shtrikman, D. Mahalu, U. Meirav, *Phys. Rev. Lett.* **1998**, *81*, 5225–5228.

[33] J. W. G. Bos, F. Faucheux, R. A. Downie, A. Marcinkova, *J. Solid State Chem.* **2012**, *193*, 13–18.

[34] J. Wang, X.-C. Liu, S.-Q. Xia, X.-T. Tao, *J. Am. Chem. Soc.* **2013**, *135*, 11840–11848.

RESEARCH ARTICLE

Thermoelectric properties and Kondo transition in the pseudo-gap metals TiNiSi and TiNiGe